Monthly Notices of the ROYAL ASTRONOMICAL SOCIETY

MNRAS **507,** 4864–4878 (2021) https://doi.org/10.1093/mnras/stab2462
Advance Access publication 2021 September 2

Radiation GRMHD simulations of M87: funnel properties and prospects for gap acceleration

Philippe Z. Yao,[1,2]★ Jason Dexter,[1,2]★ Alexander Y. Chen,[2] Benjamin R. Ryan[3] and George N. Wong[4]

[1]*Department of Astrophysical and Planetary Sciences, University of Colorado, 391 UCB, Boulder, CO 80309-0391, USA*
[2]*JILA, University of Colorado and National Institute of Standards and Technology, 440 UCB, Boulder, CO 80309-0440, USA*
[3]*CCS-2, Los Alamos National Laboratory, PO Box 1663, Los Alamos, NM 87545, USA*
[4]*Department of Physics, University of Illinois, 1110 West Green Street, Urbana, IL 61801, USA*

Accepted 2021 August 25. Received 2021 August 20; in original form 2021 February 26

ABSTRACT

We use the public code EBHLIGHT to carry out 3D radiative general relativistic magnetohydrodynamics (GRMHD) simulations of accretion on to the supermassive black hole in M87. The simulations self-consistently evolve a frequency-dependent Monte Carlo description of the radiation field produced by the accretion flow. We explore two limits of accumulated magnetic flux at the black hole (SANE and MAD), each coupled to several subgrid prescriptions for electron heating that are motivated by models of turbulence and magnetic reconnection. We present convergence studies for the radiation field and study its properties. We find that the near-horizon photon energy density is an order of magnitude higher than is predicted by simple isotropic estimates from the observed luminosity. The radially dependent photon momentum distribution is anisotropic and can be modeled by a set of point-sources near the equatorial plane. We draw properties of the radiation and magnetic field from the simulation and feed them into an analytic model of gap acceleration to estimate the very high energy (VHE) γ-ray luminosity from the magnetized jet funnel, assuming that a gap is able to form. We find luminosities of $\sim 10^{41}\,\mathrm{erg\,s^{-1}}$ for MAD models and $\sim 2\times10^{40}\,\mathrm{erg\,s^{-1}}$ for SANE models, which are comparable to measurements of M87's VHE flares. The time-dependence seen in our calculations is insufficient to explain the flaring behaviour. Our results provide a step towards bridging theoretical models of near-horizon properties seen in black hole images with the VHE activity of M87.

Key words: acceleration of particles – black hole physics – MHD – galaxies: individual: M87 – galaxies: jets.

1 INTRODUCTION

The relativistic jet launched from the centre of the elliptical galaxy M87 radiates across the radio to X-ray bands (e.g. Biretta, Sparks & Macchetto 1999; Junor, Biretta & Livio 1999; Di Matteo et al. 2003; Walker et al. 2018). Radio VLBI observations show that the jet core originates near the black hole event horizon (Hada et al. 2011). The jet is also a source of rapidly variable, very high energy TeV emission (Aharonian et al. 2006). The variability time-scale can be as short as 1–2 d (Abramowski et al. 2012), which corresponds to fewer than 10 light-crossing times of the event horizon of a black hole with mass $M_{\rm BH}\approx 6\times10^9\,\mathrm{M_\odot}$.

The physical origin of the flaring remains uncertain. During the 2008 flaring events, radio brightening and subsequent enhanced X-ray flux from the core region was detected (Acciari et al. 2009). The multiwavelength correlations together with the rapid variability suggest that the VHE γ-ray emission may originate from the jet base, close to the event horizon.

The jet is thought to be launched from the accretion flow on to M87's central, supermassive black hole (e.g. Reynolds et al. 1996; Di Matteo et al. 2003). The accretion flow is expected to be hot, geometrically thick, and optically thin at the low luminosity of M87, $L/L_{\rm Edd}\lesssim10^{-5}$ (Kuo et al. 2014), where $L_{\rm Edd}\equiv 4\pi GMm_{\rm p}c/\sigma_{\rm T}$ is the Eddington luminosity. A theoretical description of magnetized accretion (Balbus & Hawley 1991) and jet launching via the Blandford–Znajek mechanism (Blandford & Znajek 1977) can be captured in global, three-dimensional, general relativistic magneto-hydrodynamic (GRMHD) simulations (e.g. De Villiers, Hawley & Krolik 2003; Gammie, McKinney & Tóth 2003). Such simulations can be used to interpret observations of near horizon radiation from M87 (e.g. Mościbrodzka et al. 2011; Dexter, McKinney & Agol 2012; Mościbrodzka, Falcke & Shiokawa 2016; Ryan et al. 2018; Chael, Narayan & Johnson 2019; Davelaar et al. 2019; Event Horizon Telescope Collaboration et al. 2019b), especially in the context of the resolved structure at 1.3 mm (Doeleman et al. 2012; Akiyama et al. 2015; Event Horizon Telescope Collaboration et al. 2019a, c; Wielgus et al. 2020).

Unlike in the case of the Galactic Centre (Dibi et al. 2012; Drappeau et al. 2013), radiative cooling of relativistic electrons by inverse-Compton scattering and synchrotron radiation is likely important at the comparatively higher mass accretion rate of the M87 black hole system (e.g. Mościbrodzka et al. 2011). Cooling has been incorporated in GRMHD simulations of accretion on to the M87 black hole using both an M1 moment scheme (Chael et al. 2019) and a full frequency- and angle-dependent Monte Carlo treatment of the radiation field (Ryan et al. 2018). In both cases, the electrons are evolved as a separate fluid (Ressler et al. 2015), whose heating is modelled using subgrid prescriptions based on kinetic physics (e.g. Howes 2010; Rowan, Sironi & Narayan

★ E-mail: zhiyu.yao@colorado.edu (PZY); jason.dexter@colorado.edu (JD)

2017). Using a specific electron heating model, radiation GRMHD simulations can self-consistently evolve the radiation field and model the observed spectrum due to synchrotron emission and Compton scattering.

The TeV VHE emission, on the other hand, is produced by electrons accelerated to very high energies ($\gamma_e \gtrsim 10^6$). One proposed acceleration site could be near the event horizon, where a charge-starved 'gap' region could form within the magnetically dominated jet near the pole (the 'funnel') (Levinson & Rieger 2011). Inside this gap region, particles would be accelerated by an unscreened electric field $E_\parallel$ (parallel to the magnetic field in the jet) to Lorentz factors of $\gamma_e > 10^6$ and emit γ-rays through inverse-Compton scattering with the photons produced in the disc. Some of these γ-rays convert into pairs to sustain the electric current in the jet funnel, while the rest escape to infinity and produce the observed emission. Since $E_\parallel$ is explicitly zero in ideal GRMHD simulations, parallel acceleration cannot be captured self-consistently. Simulations that treat $E_\parallel \neq 0$ would have to account for highly non-thermal particle distributions. Recently, this process was studied through first-principles local and global Particle-in-Cell (PIC) kinetic simulations (e.g. Chen, Yuan & Yang 2018; Levinson & Cerutti 2018; Chen & Yuan 2020; Crinquand et al. 2020; Kisaka, Levinson & Toma 2020a). These PIC simulations typically neglect modeling the accretion disc and assume simple configurations, such as a monopolar magnetic field and an isotropic background photon field. However, the results of the PIC studies suggest that the VHE luminosity and spectrum depend crucially on the surrounding magnetic and radiation field structure. Therefore, it is necessary to consider them in the context of global GRMHD simulations in order to make meaningful predictions about the VHE γ-ray emission from M87.

Here we take a step towards bridging global calculations of accretion on to M87 with local kinetic models of gap acceleration. We carry out three-dimensional, global, radiation GRMHD simulations of M87 using the public EBHLIGHT code (Ryan, Dolence & Gammie 2015; Ryan et al. 2019). The frequency-dependent radiation field is evolved using a Monte Carlo method. We use the simulations to study the fluid and radiation field in the dense accretion flow (Section 2) and evacuated funnel (Section 3) regions. We next study models of plasma production in the funnel, either through pair production by photons emitted in the accretion flow (Section 4.1) or by high-energy γ-ray photons emitted by particles accelerated in a gap (Section 4.2). Our results have implications for both PIC simulations of kinetic processes in the magnetosphere and the feasibility of near horizon particle acceleration from M87 (Section 5).

2 SIMULATIONS

We carried out radiation GRMHD simulations using version 1.0 of the public code EBHLIGHT[1] (Ryan et al. 2015, 2017). EBHLIGHT uses the HARM scheme for conservative ideal GRMHD (Gammie et al. 2003; Noble et al. 2006) and implements a Monte Carlo treatment of the anisotropic, frequency-dependent radiation field. The electron entropy is evolved separately, with a heating rate calculated as a fraction of the dissipated grid-scale energy according to a subgrid prescription (Ressler et al. 2015). Synchrotron emission and self-absorption and Compton scattering are included self-consistently.[2]

[1] https://github.com/AFD-Illinois/ebhlight.

[2] We did not include bremsstrahlung, which is subdominant in terms of cooling but could contribute to the high-energy component of the SED (Yarza et al. 2020).

The integrations are done explicitly with a time-step limited by the light-crossing time of the smallest zone. We find that the fiducial simulations presented here are approximately four to five times more computationally expensive than non-radiative GRMHD simulations performed at the same grid resolution.

2.1 Simulation setup

The simulations were initialized from a Fishbone–Moncrief torus with an inner radius of $r_{\rm in} = 12\,r_{\rm g}$, a pressure maximum radius of $r_{\rm max} = 25\,r_{\rm g}$, and a dimensionless black hole spin parameter $a \equiv Jc/GM^2 = 0.9375$, where $r_{\rm g} = GM/c^2$, J is the angular momentum of the hole, and $M_{\rm BH} = 6.5 \times 10^9\,{\rm M}_\odot$ (Gebhardt et al. 2011; Event Horizon Telescope Collaboration et al. 2019c). The grid resolution was $320 \times 256 \times 160$, and simulations were carried out in modified Kerr–Schild coordinates (Porth et al. 2019), which concentrate θ resolution towards the mid-plane at small radius and allow a larger time-step. The torus is seeded with a magnetic field chosen to accumulate weak (SANE) or strong (dynamically important, MAD) magnetic fields on the central black hole. We used four separate schemes for electron heating, based on the results of kinetic calculations. We considered turbulent heating as realized in gyrokinetics calculations (Howes 2010, hereafter H10; Kawazura, Barnes & Schekochihin 2019, hereafter K19) and heating by magnetic reconnection as realized in particle-in-cell calculations with a modest guide field (Rowan et al. 2017, hereafter R17; Werner et al. 2018, hereafter W18). The gyrokinetic turbulence prescriptions introduce a strong magnetization dependence into the electron heating fraction (electrons receive a greater fraction of heating in more strongly magnetized regions), while the reconnection prescriptions are more uniform (see e.g. Chael et al. 2019). In the non-radiative case, multiple electron species can be evolved in parallel to explore different heating models during a single simulation (e.g. Ressler et al. 2017). Here, a new simulation is required for each subgrid prescription since the radiation field is coupled to the MHD and depends on the electron temperature. A ceiling was imposed on the magnetization parameter, $\sigma = b^2/\rho \leq 50$, to allow for stable evolution of the magnetically dominated polar regions. This procedure artificially injects mass at high temperature. To avoid generating luminosity from this injected material, regions where $\sigma > 1$ or the dimensionless electron temperature $kT_e/m_ec^2 > 10^3$ do not contribute to the emission, absorption, or scattering.

We first ran an initial, non-radiative MAD GRMHD simulation to $t = 4.2 \times 10^3\,r_{\rm g}/c$ using the W18 heating prescription. The radiation was then turned on, and we ran four simulations using each of the H10/K19/W18/R17 electron heating prescriptions. The simulation mass unit was chosen to approximately match the observed $\simeq$ 1-Jy, 230-GHz flux density of M87. This choice determines the time-averaged mass accretion rate on to the black hole. After turning on radiation, the system re-equilibrates after a dynamical time of $\lesssim 10^2\,r_{\rm g}/c$. For the SANE simulations, we started with a radiative GRMHD simulation also using the W18 prescription. We then restarted from that solution at $t = 5 \times 10^3\,r_{\rm g}/c$, again running four simulations using each of the four electron heating prescriptions. The procedure used for the MAD case is more efficient, since at early times a longer time-step can be taken in the absence of radiation and the execution time per time-step is shorter. All simulations were run for a total duration of $\simeq 8 \times 10^3\,r_{\rm g}/c$.

Fig. 1 shows the time evolution of the (positive) mass accretion rate $\dot{M}$ and the dimensionless magnetic flux on the horizon $\phi = \sqrt{4\pi}\Phi/\sqrt{\dot{M}}$, both in code units with $GM = c = 1$. In the MAD case, the magnetic flux ramps up and saturates at a value of $\phi \simeq 60$–80,

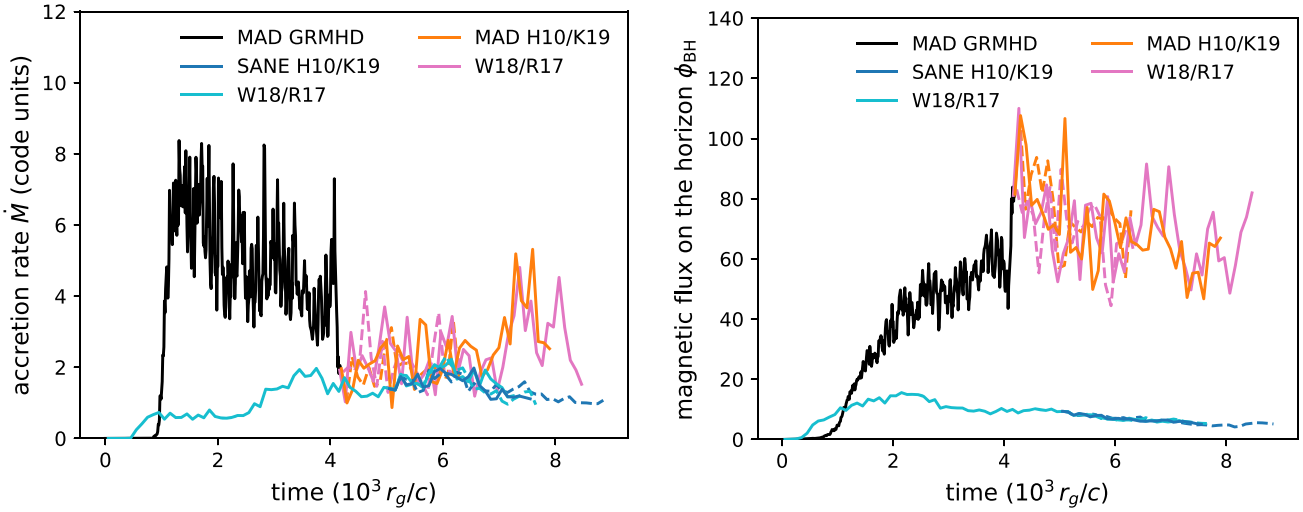

Figure 1. Time series of mass accretion rate and dimensionless magnetic flux from the simulations as measured at the event horizon. The MAD radiation GRMHD simulations were all restarted from an initial non-radiative GRMHD calculation at a time $t \simeq 4 \times 10^3\, r_{\rm g}/c$ (black lines).

Table 1. Properties of the EBHLIGHT simulations in this work averaged over the final $2000\, r_{\rm g}/c$ of each simulation ($t \simeq (6\text{–}8) \times 10^3\, r_{\rm g}/c$).

Magnetic field	Electron model	$\phi_{\rm BH}$	$\langle B_r^2\rangle/\langle B_\phi^2\rangle$	$\langle Q_\theta\rangle$	$\langle Q_\phi\rangle$	$\langle\beta\rangle$	$N_{\rm sph}$ (10^7)	$\langle Q_{\rm emit}\rangle$	$\langle\beta_{\rm rad}\rangle$
SANE	H10	6.3	0.15	22.5	23.6	24.7	7.9	225.0	145.2
SANE	W18	6.6	0.15	25.2	26.2	19.1	4.2	347.5	33.0
SANE	R17	6.4	0.14	23.6	25.0	21.1	3.9	252.6	55.5
SANE	K19	5.1	0.14	18.9	20.2	30.9	3.7	318.8	773.0
MAD	H10	64.7	0.26	70.6	64.3	5.7	7.1	12.3	9.4
MAD	W18	67.6	0.23	61.0	56.1	7.7	6.5	110.5	18.5
MAD	R17	71.4	0.33	121.8	84.7	4.3	4.9	19.8	9.8
MAD	K19	73.1	0.26	96.6	79.8	4.4	5.8	15.7	12.1

Notes. The dimensionless magnetic flux $\phi_{\rm BH}$ is measured at the event horizon, and the other quantities are averaged over $4\text{–}10 r_{\rm g}$. Here, $\langle Q\rangle$ denotes the average MRI resolution quality factors, $\langle\beta\rangle$ and $\langle\beta_{\rm rad}\rangle$ are the plasma and radiation β, and $N_{\rm sph}$ is the number of superphoton packets.

consistent with past results (Tchekhovskoy, Narayan & McKinney 2011; McKinney, Tchekhovskoy & Blandford 2012). The accretion rate quickly reaches a maximum, then slowly decreases. We note that the large drop around $\simeq 4 \times 10^3\, r_{\rm g}/c$ occurs before radiation is turned on, and we occasionally see similar features in other, non-radiative MAD GRMHD simulations (e.g. Dexter et al. 2020). In the SANE case, the accretion rate reaches a maximum more slowly since the magnetorotational instability (MRI; Balbus & Hawley 1991) is not well resolved in the outer torus where most of the mass is contained (e.g. Liska et al. 2018). The magnetic flux saturates at a lower value of $\phi \simeq 5$. We define the equilibrium radius as the outermost location where the elapsed time is longer than the local inflow time, $t_{\rm inflow} = r/|v^r|$ (Narayan et al. 2012). According to that criterion, inflow equilibrium is established out to $r_{\rm eq} \simeq 15\, r_{\rm g}$, $13\, r_{\rm g}$ for the MAD, and SANE simulations by $7 \times 10^3\, r_{\rm g}/c$.

The radiation field in EBHLIGHT comprises a large number of Monte Carlo samples (superphotons), each with a particular position and wavevector and corresponding to a large number of individual photons. One quality factor for the radiation field is the number of superphotons emitted locally in one cooling time due to synchrotron radiation (Miller et al. 2019), $Q_{\rm emit} = t_{\rm cool}\, N_{\rm emit}/\Delta t$. Here, the cooling time $t_{\rm cool} = u_{\rm g}/\Lambda$ is the ratio of the energy density of the gas to the cooling rate, and the average rate of superphoton emission is $N_{\rm emit}/\Delta t$. A minimal value of $Q_{\rm emit} \gtrsim 1$ is needed to avoid supercooling events, during which a simulation zone cools too quickly and releases a significant fraction of its internal energy in a single simulation time-step. In all of our simulations, we find density-weighted shell-averaged values $\langle Q_{\rm emit}\rangle \simeq 10\text{–}200$ near the black hole (Table 1). An analogous quality factor can be defined for scattering events (inverse-Compton cooling). This factor decreases rapidly with decreasing radius, becoming <1 very close to the event horizon. We study the properties of both quality factors in Appendix A as a function of the number of superphotons used in the calculation. The values found here appear satisfactory to provide a converged description of the time- and shell-averaged radiation field. In Appendix B, we show that radiative cooling reduces the average near-horizon electron temperature by factors of $\simeq 2\text{–}5$.

Azimuthally averaged snapshot 2D maps of selected fluid and radiation quantities from the H10/W18 electron heating models are shown in Fig. 2. The H10 prescription results in a colder accretion flow and hotter funnel. The electron temperatures of our MAD models are somewhat higher than their SANE counterparts. Radiation is more important than gas pressure over a large swath of the funnel for the MAD H10 and SANE W18 cases, and the gas pressure is in general overestimated there due to the influence of numerical floors. Our SANE H10 simulation radiates a lower luminosity by a factor of $\simeq 2$. If we increased $\dot{M}$ to match the luminosity of the other simulations, the effect of radiative cooling would be stronger than found here.

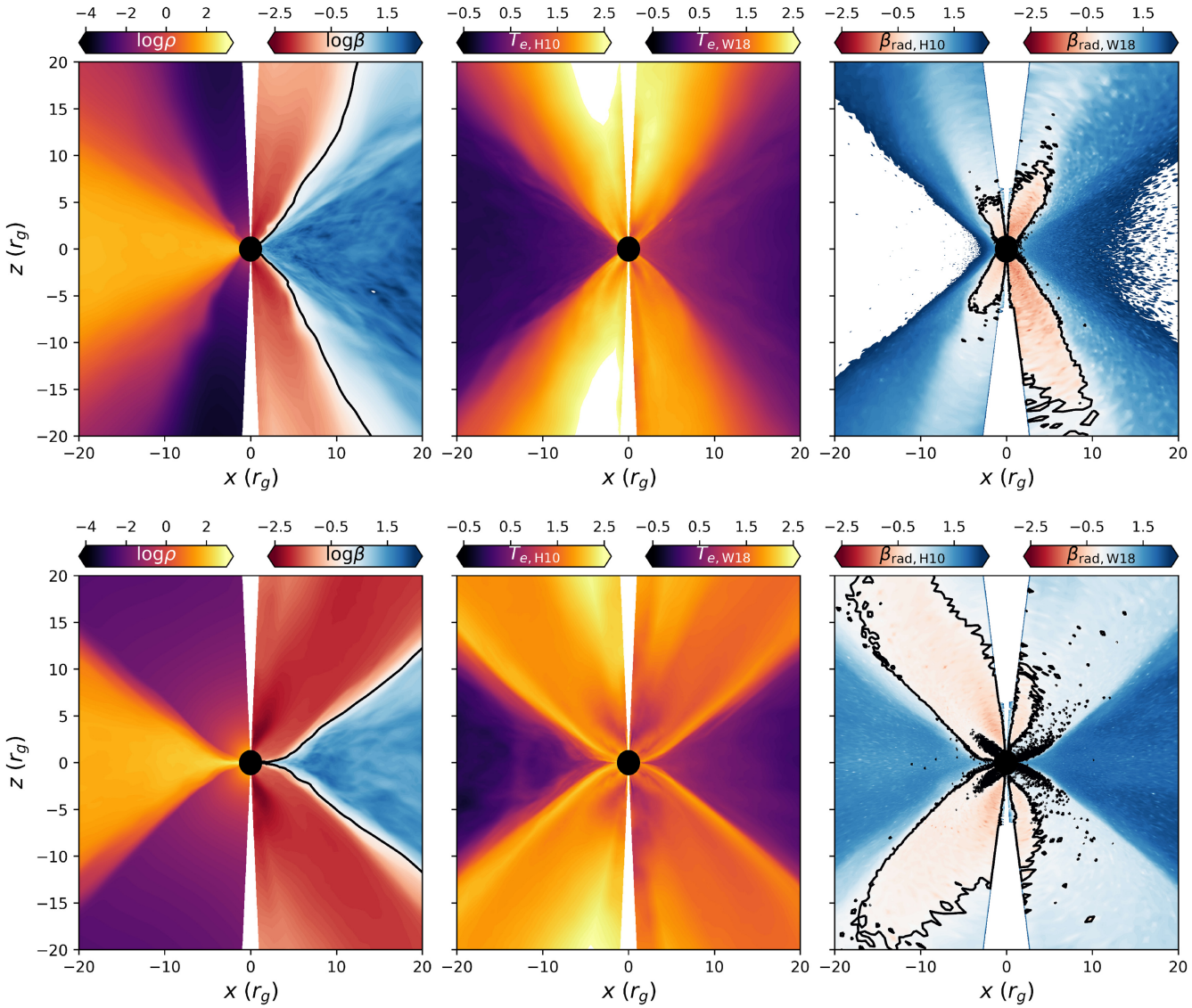

Figure 2. Azimuthally averaged mass density ρ (in code units) and ratio of gas to magnetic pressure β (left-hand panel), electron temperatures T_e for the H10 and W18 heating models (in units of $m_e c^2/k$, middle panel), and gas to radiation pressure ratio β_{rad} (right-hand panel) for SANE (top) panel and MAD (bottom panel) simulations. We show only the W18 maps of ρ and β, since they are indistinguishable by eye from those of the H10 simulations. The black solid lines mark where $\beta = 1$.

We calculate observed spectra from our simulations by collecting superphoton packets at a radius $r = 40\,r_g$. Fig. 3 shows spectra for a low inclination observer. The spectra are binned over the final $500\,r_g/c$ of simulation time, over all azimuthal angles, and over low inclination angles relative to the black hole spin axis of 0°–25° to be consistent with the inferred jet viewing geometry of M87 (e.g. Biretta et al. 1999). Synchrotron radiation produces an initial peak near THz frequencies, with a broader peak in models with a wider range of temperatures for the radiating electrons (SANE H10/K19 and MADs). The spacing of the Compton bumps is set by the typical electron temperature in the accretion flow, where the scattering optical depth is largest. The relatively hot and dense accretion flow in SANE W18/R17 models produces a large X-ray luminosity from inverse-Compton scattering and exceeds the total observed X-ray luminosity of M87 (data points compiled by Prieto et al. 2016, see references therein). With a purely thermal distribution of electrons, our models can match the observed sub-mm and potentially X-ray luminosity. They underproduce the infrared emission, which could arise from synchrotron jet (Perlman et al. 2001) or thermal accretion disc (Prieto et al. 2016) emission. In the case of synchrotron radiation, a non-thermal tail to the distribution function is likely responsible (Davelaar et al. 2019). Mass accretion rate values, bolometric luminosities, jet powers, and their efficiencies are listed in Table 2. Our high-spin MAD models have radiative efficiencies of $\simeq 10$ per cent and jet efficiencies > 100 per cent. The high jet efficiencies are consistent with past work (e.g. Tchekhovskoy et al. 2011) and demonstrate spin energy extraction from the black hole.

3 FUNNEL MAGNETIC AND RADIATION FIELD PROPERTIES

In order to study the local particle acceleration inside the jet funnel, we need to understand properties of the radiation field and the magnetic field within the jet. We begin the analysis by

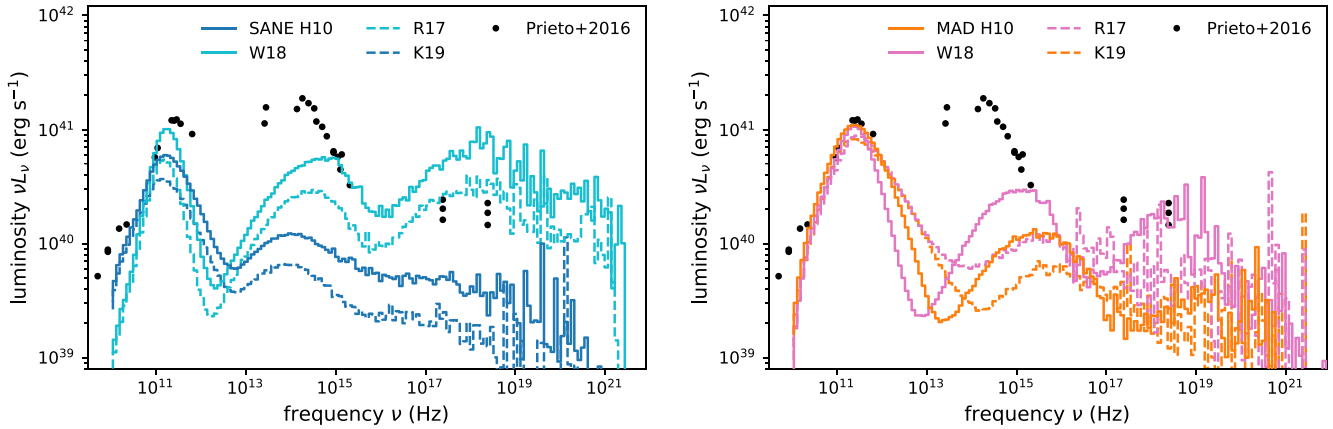

Figure 3. Spectra averaged over the last $500\,r_g/c$ from our SANE (left-hand panel) and MAD (right-hand panel) models compared to M87 data (Prieto et al. 2016 and references therein). The MAD R17 model also shows significant spectral variability, which causes a temporary increase in the infrared luminosity by a factor of several above the quiescent average shown here.

Table 2. Average properties of the EBHLIGHT simulations presented here averaged over the final $2000\,r_g/c$ of each simulation.

Magnetic field	Electron model	$\dot{M}_{-4}$	$L_{\rm scat}/L_{\rm emit}$	$L_{\rm bol,\,42}$	$L_{\rm jet,\,42}$	$L_{\rm bol}/\dot{M}c^2$	$L_{\rm jet}/\dot{M}c^2$
SANE	H10	7.2	0.8	0.4	1.0	0.009	0.024
SANE	W18	8.1	4.3	1.2	0.9	0.026	0.019
SANE	R17	6.8	3.8	0.9	1.5	0.023	0.040
SANE	K19	5.7	0.6	0.2	0.9	0.006	0.027
MAD	H10	1.6	0.4	1.0	17.1	0.111	1.836
MAD	W18	3.5	1.2	1.5	40.2	0.075	2.020
MAD	R17	3.0	0.9	1.6	38.9	0.095	2.268
MAD	K19	1.2	0.3	0.6	17.0	0.094	2.461

Notes. The accretion rate $\dot{M}$ is measured at the event horizon. The bolometric luminosity is measured at $40\,r_g$, and the jet power $L_{\rm jet}$ is measured at $100\,r_g$. $L_{\rm scat}/L_{\rm emit}$ is the ratio of luminosities produced by scattering to those produced by emission. Luminosities L_{42} are reported in units of 10^{42} erg s^{-1}, and $\dot{M}_4$ is the mass accretion rate in units of 10^{-4} M$_\odot$ yr^{-1}.

defining a general jet boundary in our simulation results using an azimuthally averaged magnetization parameter $\sigma = \langle b^2\rangle/\langle\rho\rangle$, defined with the magnetic field b and matter density ρ. We define our jet to be the magnetically dominated region where $\sigma \geq \xi$. The choice $\xi = 1$ of McKinney et al. (2012) includes the turbulent accretion disc of our MAD simulations. Since it seems unlikely that an empty, unscreened gap could form there, we instead chose $\xi = 5$ (Fig. 4). By our definition, SANE simulations have a narrower funnel than MAD simulations. Because of the relatively mild differences produced by these electron heating schemes, we will use H10 and W18 to study the differences in the remainder of this section.

3.1 Radiation energy density and magnetic field structure

The radiation physics sector of the calculation is not scale-free, so the length (and time) and density invariance of metric and GRMHD evolution equations must be broken. In our simulation, the relevant length and time-scales are both set by the mass of the central black hole: r_g and r_g/c. We set the final (density) scale of each simulation by simultaneously rescaling the rest mass density, internal energy, and magnetic field strength until the simulations produce the observed 1.3-mm flux density of M87 ($\simeq 1$ Jy for $D = 16.8$ Mpc; Tully 1988). We compute $\langle x\rangle_f(z)$, the height-dependent, funnel-averaged profile of a variable x, by calculating its shell-average:

$$\langle x\rangle_f = \frac{\sum_{j=0}^{2\pi}\sum_{k=\theta_{k1}}^{\theta_{k2}} x_{jk}\sqrt{-g_{jk}}}{\sum_{j=0}^{2\pi}\sum_{k=\theta_{k1}}^{\theta_{k2}}\sqrt{-g_{jk}}}, \quad (1)$$

where $\sqrt{-g}$ is the metric determinant.

We extract the photon number density $n_{\rm s}$, the radiation energy density $u_{\rm rad}$, the background current density squared $j^2 = j^\mu j_\mu$ ($j^\mu = F^{\mu\nu}{}_{;\,\nu}$ and $F^{\mu\nu}$ is the electromagnetic field tensor), and the magnetic field strength squared $b^2 = b^\mu b_\mu$ (b^μ is the magnetic field four-vector) from the simulation data. These quantities are converted into cgs units and further multiplied by a factor of $\sqrt{4\pi}$ to convert from the Heaviside–Lorentz into Gaussian field convention.

Fig. 5 shows azimuthally averaged maps of the magnitude of the current density. The choice of electron heating scheme has little effect on the background current density because the radiation field is not strong enough to influence it. The current density is a factor of several higher in the MAD simulations than in the SANE ones.

Fig. 6 shows vertical profiles of the radiation energy density and average photon energy. Both decay as power laws with height. At small radii, the radiation energy density is higher than simple estimates predicted by the observed luminosity assuming isotropy, e.g. $u_{\rm rad}$ increases more quickly towards the black hole than $\propto z^{-2}$. This is likely due to relativistic effects, e.g. the gravitational redshift.

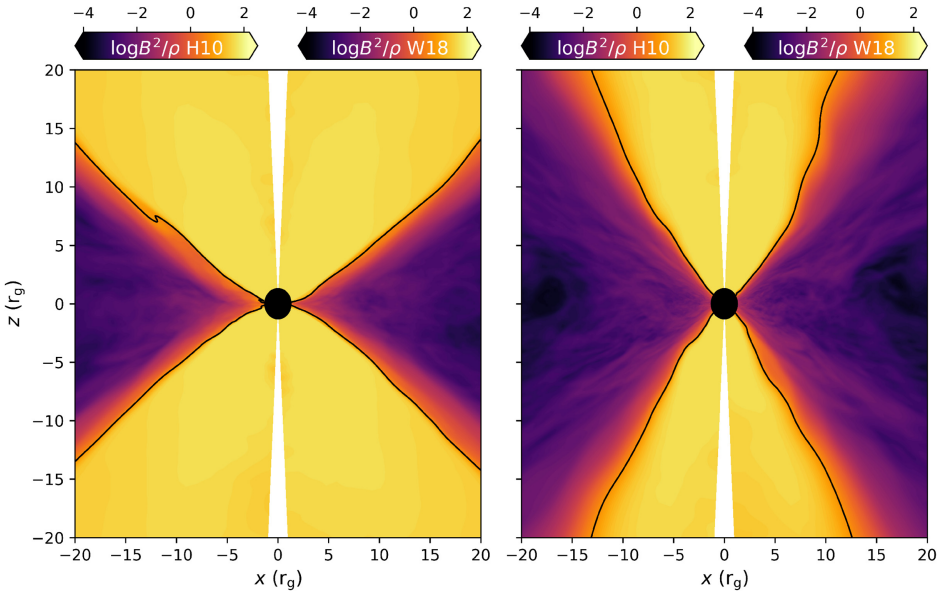

Figure 4. Azimuthally averaged magnetization (ratio of magnetic to rest mass energy density) for sample MAD (left-hand panel) and SANE (right-hand panel) simulations. The black solid line marks our adopted definition of the jet boundary ($\sigma \geq 5$).

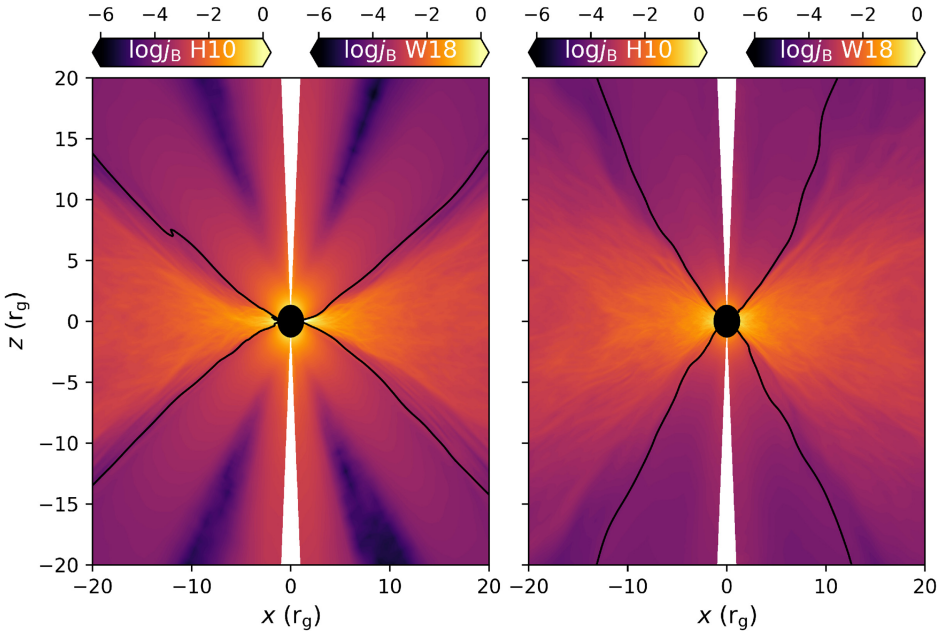

Figure 5. Log contour plots of background current density for MAD simulations (left-hand panel) and SANE simulations (right-hand panel) with H10 or W18 electron heating schemes. The black solid line marks the jet boundary defined with $\sigma \geq 5$.

At $\sim 3r_g$, the photon number density $n_s \simeq 10^{14}$–10^{15} cm^{-3} and $u_{rad} \simeq 0.1$–10 erg cm^{-3}. The high end of the ranges corresponds to MAD simulations.

3.2 Photon distribution

We also measured the photon distribution in the funnel region and around the black hole. For a single time slice in each model, we output the coordinate positions x^μ and wave four-vectors k^μ of all superphoton packets in the simulation. We then transformed the four-vector components from the code coordinate basis to the orthonormal, zero angular momentum observer (ZAMO; Bardeen, Press & Teukolsky 1972) frame.

In addition to photon distributions, we calculate average cooling region locations and sizes in SANE and MAD simulations. In each simulation, we extract the volumetric radiative energy exchange rate due to emission J_{em} and find its mean and standard deviation in radius and polar angle, assuming axisymmetry, with

$$r_c = \frac{\sum_{r,\theta,\phi} J_{em} \times r}{\sum_{r,\theta,\phi} J_{em}}, \quad \Delta r_c = \frac{\sum_{r,\theta,\phi} J_{em} \times r^2}{\sum_{r,\theta,\phi} J_{em}}, \tag{2}$$

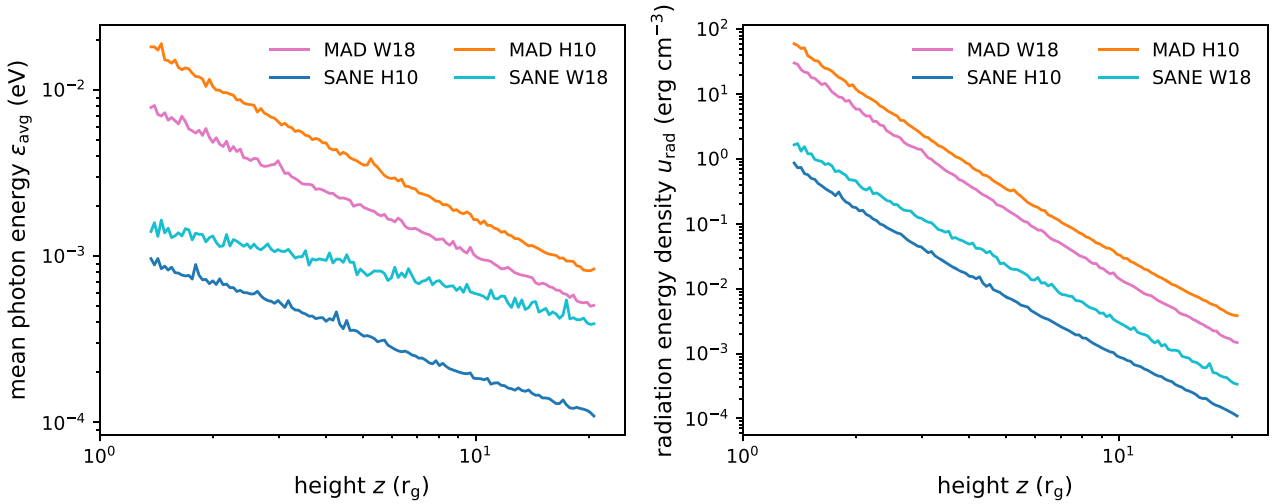

Figure 6. Average photon energy ($\epsilon_{avg} = u_{rad}/n_s$, left-hand panel) and radiation energy density (u_{rad}, right-hand panel) plotted against height for MAD simulation with W18 (pink) or H10 (orange) electron heating schemes and SANE simulation with W18 (cyan) or H10 (blue) electron heating schemes.

Table 3. Photon emission region location and size in radius and polar angle for sample MAD and SANE simulations.

Magnetic field	Electron model	r_c (r_g)	Δr_c (r_g)	θ_c	$\Delta\theta_c$
SANE (north)	H10	1.7	0.39	0.41π	0.05π
SANE (south)	H10	1.7	0.40	0.57π	0.05π
MAD	W18	1.7	0.49	0.51π	0.03π

Note. The SANE case is split into contributions from above (north) and below (south) the equatorial plane.

and similarly

$$\theta_c = \frac{\sum_{r,\theta,\phi} J_{em} \times \theta}{\sum_{r,\theta,\phi} J_{em}}, \quad \Delta\theta_c = \frac{\sum_{r,\theta,\phi} J_{em} \times \theta^2}{\sum_{r,\theta,\phi} J_{em}}. \tag{3}$$

As shown in Table 3, the average photon emission radii for all models are very close to the event horizon. Photons in the MAD W18 simulation are emitted in a narrow polar angle range around the equatorial plane. In the SANE H10 simulation, we find that photons are emitted by two similar structures above and below the disc. This is due to the fact that the H10 electron heating scheme results in a relatively cold disc in this SANE simulation (cf. Mościbrodzka et al. 2016; Ressler et al. 2017), causing the synchrotron emission to peak at higher latitudes where the temperatures are higher.

Fig. 7 shows the photon directions in the vicinity of the black hole as observed in the ZAMO frame. Here, the funnel region is defined as $\theta \geq 0.3\pi$, which is close to where $\sigma \geq 5$, and the disc region is taken to be within 0.1π of $\theta = \pi/2$. We report the angle between each photon's k^z and k^R components expressed in cylindrical coordinates in the ZAMO frame. Photons are emitted at small radius close to the equatorial plane ($\theta_{KS} \sim \pi/2$). In those locations, the photon distribution is nearly isotropic. Outside the emission region, photons preferentially travel outwards. Additionally, no photons are emitted from inside the funnel region where the MHD density and internal energy are unreliable. At small heights above the event horizon, photons are preferentially directed inwards towards the black hole as a result of light bending. This bending effect weakens with distance, resulting in an increasing fraction of outgoing photons with height until they are nearly all outgoing ($r \gtrsim 6r_g$). SANE simulations seem less beamed in both the funnel and the equatorial plane in part because of the presence of two emission regions above and below the equatorial plane. Fig. 8 shows a schematic diagram illustrating the expected radiation field from compact, axisymmetric emission regions placed in the primary emission regions we have identified for the MAD W18 and SANE H10 simulations. The measured radial dependence of the radiation field anisotropy is consistent with the measured location of the emission region.

One promising site for gap formation is near the null surface around $r \simeq 2r_g$ (Chen et al. 2018; Chen & Yuan 2020; Kisaka, Levinson & Toma 2020b). At such small radii, the funnel radiation field is composed of nearly equal numbers of ingoing and outgoing photons. As a result, the net outward radiative flux is $F \ll 4u_{rad}/c$ and an analytic estimate of u using the observed luminosity L underestimates the photon number density and energy density by up to one to two orders of magnitude.

4 FUNNEL PARTICLE DENSITY AND PROSPECTS FOR GAP FORMATION

In the previous section we studied the radiation and magnetic field properties of the funnel region, which can be reliably measured using radiation GRMHD simulations. The matter content inside the funnel, however, is dominated by artificially injected mass and energy ('floors') needed for a stable evolution of the code. In reality, a physical mechanism is required to supply the plasma needed in the jet funnel. Here we discuss two physical scenarios for particle loading in the funnel region and their implications for particle acceleration.

4.1 Pair production from annihilation of photons produced in the accretion flow

Photons produced by the background radiation field of the accretion flow may interact with one another and convert into electron–positron pairs. This 'drizzle' pair creation process provides a mechanism to mass-load the otherwise evacuated funnel. Photons with energies $h\nu > m_e c^2$ ($\gtrsim 1$ MeV) are produced in radiation GRMHD simulations by inverse-Compton scattering. Post-processing calculations of the pair production process can provide quantitative estimates of the funnel particle density (e.g. Mościbrodzka et al. 2011; Wong, Ryan & Gammie 2021).

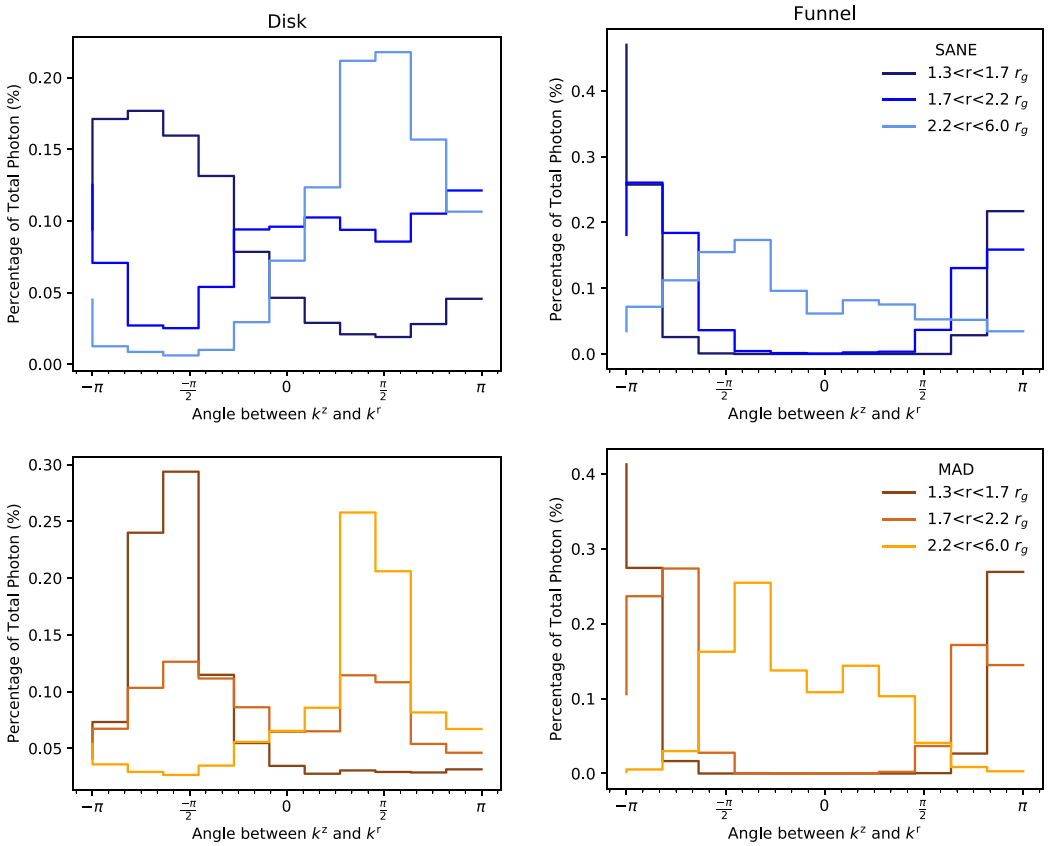

Figure 7. Relative photon direction in height and cylindrical radius measured as $\alpha = \mathrm{sign}(k^z) \times \cos^{-1}(k^z/\sqrt{k^{R\,2} + k^{z\,2}})$ in the funnel region and as $\alpha = \mathrm{sign}(k^R) \times \cos^{-1}(k^z/\sqrt{k^{R\,2} + k^{z\,2}})$ in the equatorial plane, where k^i are measured in the orthonormal ZAMO frame. The distributions are shown for SANE H10 (top panel) and MAD W18 (bottom panel) simulations in equatorial plane (left-hand panel) and funnel region (right-hand panel). Lighter colours represents greater radial distance of photon packets from the black hole. In general, the radiation field is anisotropic and varies from predominantly inwards to predominantly outwards trajectories within $1.4 \lesssim r \lesssim 6\,r_{\rm g}$.

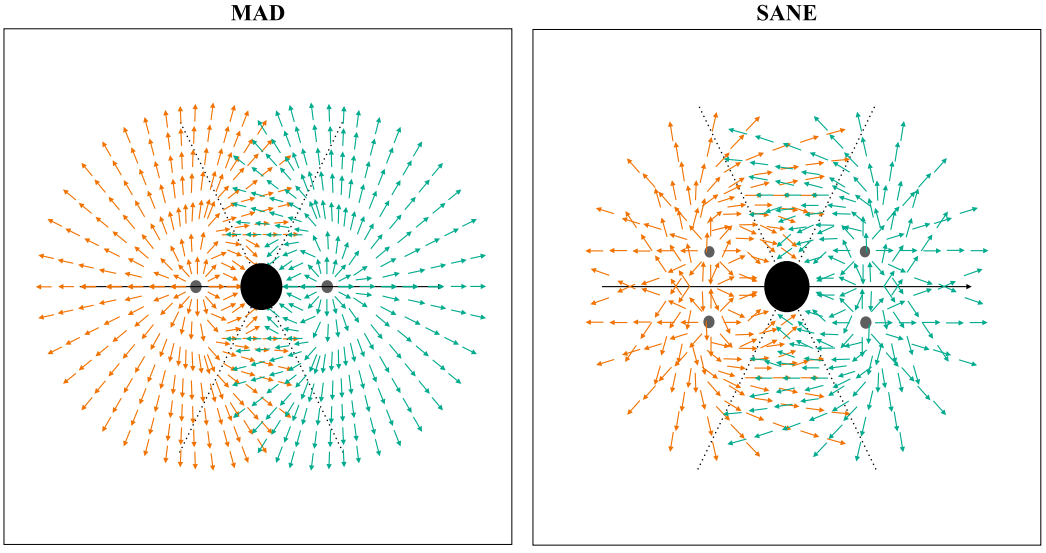

Figure 8. Schematic diagram showing the approximate photon distributions expected for emission from a ring at 1.7–$2r_{\rm g}$ in the equatorial plane (left-hand panel) and for two similar rings elevated some height and symmetric about the equatorial plane. These toy geometries are motivated by the measured emission region properties for MAD (left-hand panel) and SANE (right-hand panel) simulations listed in Table 3, and help explain the anisotropic photon distributions shown in Fig. 7.

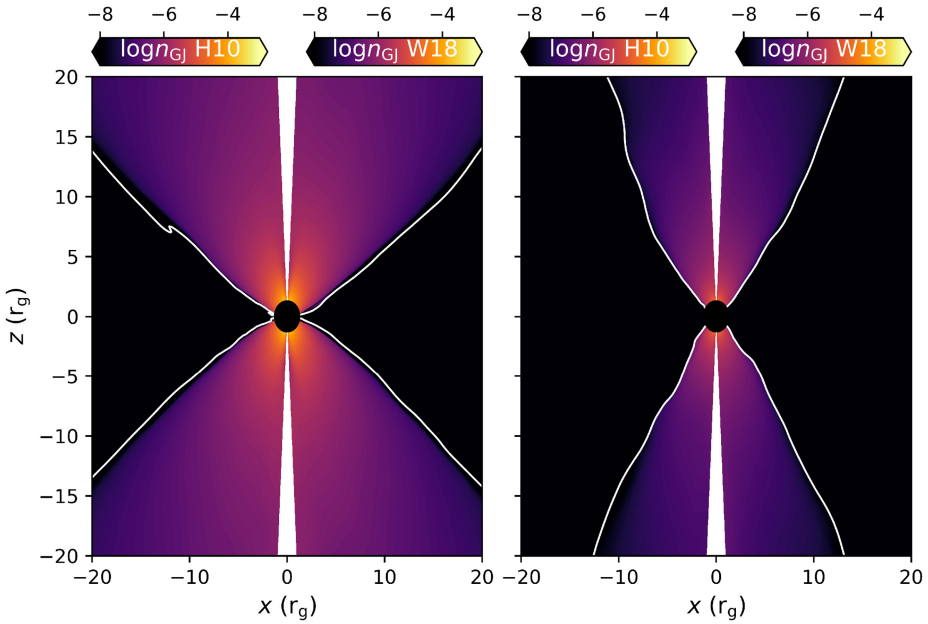

Figure 9. Log contour plots of funnel Goldreich–Julian density (n_{GJ}) in units of cm^{-3} for MAD simulations (left-hand panel) and SANE simulations (right-hand panel) with different electron heating schemes. The white solid line marks the jet boundary defined as $\sigma \geq 5$.

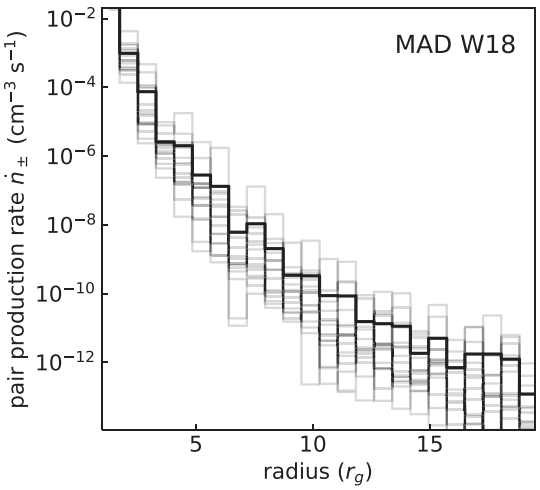

Figure 10. Photon–photon pair-production rate as a function of height at one pole ($\theta \lesssim 5^\circ$) for the MAD W18 simulation. The thin grey lines show the result from the photon distribution in azimuthal wedges of $\Delta\phi = 22.^\circ5$ at a snapshot in time, and the thick black line is their average.

The required minimum charge density to screen the electric is the Goldreich–Julian density (e.g. Wong et al. 2021):

$$n_{GJ} = \frac{-u^\mu j_\mu}{ec^2}, \tag{4}$$

[13] where u^μ is the four-velocity of the fluid and j_μ is the four-current. Fig. 9 shows azimtuhally averaged maps of n_{GJ} inside the funnel. The maximum values of $\simeq 10^{-4}$ cm^{-3} are approximately eight orders of magnitude lower than particle densities in the accretion flow. This corresponds to an electron magnetization parameter $\sigma_{GJ} \sim 10$.

Following Mościbrodzka et al. (2011) and Wong et al. (2021), we estimated the pair-production rate from drizzle. From EBHLIGHT superphoton four-momenta k^μ recorded at a single snapshot in time, the pair production rate is estimated as

$$\dot{n}_\pm = \frac{1}{2}\sum_{ij} \frac{w_i w_j}{(\sqrt{-g}\ \Delta^3 x)^2} \frac{k_i^\mu k_{j,\mu}}{k_{0,j}\, k_{0,i}} \sigma_{\gamma\gamma}\, c, \tag{5}$$

where $\sigma_{\gamma\gamma}$ is the pair-production cross-section (e.g. Breit & Wheeler 1934), w_i is the number of photons within each Monte Carlo superphoton sample, and the sum is performed over all pairs of superphotons. For computational efficiency, we take the sum i to be only over photons exceeding the pair threshold, with energies $>0.5 m_e c^2$, while the sum j is taken over all photons. The pair drizzle calculation is performed using a short, dedicated `ebhlight` calculation with $\sim 10^{10}$ superphoton packets in order to provide a resolved sample of the high-energy radiation field. We carry out the calculations at one snapshot in time using a grid distinct from that used for the fluid, consisting of $24 \times 32 \times 16$ zones evenly spaced in r, θ, and ϕ in Kerr–Schild coordinates. The values of $\sqrt{-g}$ and Δx above refer to those calculated at the centres of these new zones and to their total sizes.

Fig. 10 shows the result near the pole for the MAD W18 model, where $\dot{n}\, r_g/c \sim 0.1$ cm^{-3} at $r \simeq 3\, r_g$. For $n_\pm \sim \dot{n}\, r_g/c$, these results imply $n_\pm/n_{GJ} \gtrsim 10^3$–$10^4$, which is sufficient to screen electric fields and prevent gap formation. The steep decline in pair-production rate with radius also matches the results of previous work (Mościbrodzka et al. 2011). Wong et al. (2021) further derived a fitting formula where $\dot{n}_\pm \sim \dot{m}^5$ for our physical regime of interest. This suggests that a change in mass accretion rate by factors of $\gtrsim 5$ could be sufficient to trigger gap formation in the MAD W18 model. Typically, $\dot{M}$ varies by factors of $\simeq$ 2–3 in GRMHD simulations.

4.2 Luminosity estimate in case of gap formation

Based on the estimates above, sufficient charge carriers are likely available to screen electric fields in the funnel region. Since a moderate change to the accretion flow or jet could plausibly result in regions with $n_\pm/n_{GJ} < 1$, we estimate the γ-ray luminosity from a gap that forms under such conditions. Chen et al. (2018) used time-

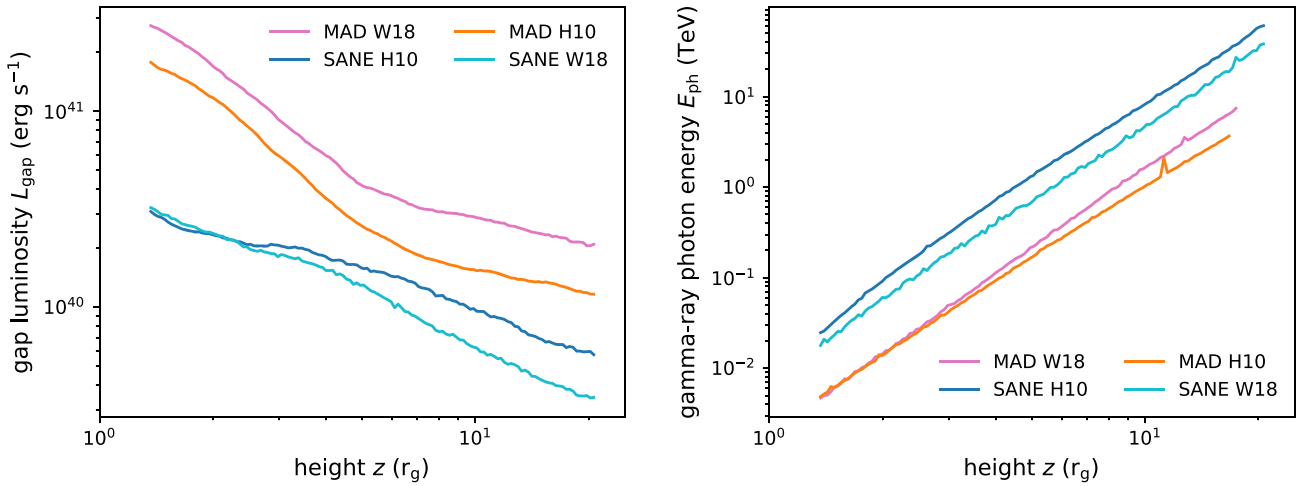

Figure 11. Time-averaged gap luminosity (left-hand panel) and maximum photon energy (right-hand panel) as functions of radius for MAD simulation with W18 (pink) or H10 (orange) electron heating schemes and SANE simulation with W18 (cyan) or H10 (blue) schemes.

Table 4. Characteristic parameters of four sets of simulation results averaged between 2 and $3r_{\rm g}$.

Parameters	MAD W18	MAD H10	SANE W18	SANE H10
$n_{\rm s}$ (cm^{-3})	3.7×10^{14}	3.6×10^{14}	1.2×10^{14}	8.6×10^{13}
$l_{\rm IC}$	4.6×10^{9}	5.0×10^{9}	1.5×10^{10}	2.0×10^{10}
τ_0	2.3×10^{5}	2.2×10^{5}	7.0×10^{4}	5.3×10^{4}
$u_{\rm rad}$ (erg cm^{-3})	2.9	3.4	0.78	0.30
$\epsilon_{\rm min}/m_{\rm e}c^2$	1.8×10^{-9}	1.9×10^{-9}	1.5×10^{-9}	7.2×10^{-10}
$\epsilon_{\rm min}$ (erg)	1.4×10^{-15}	1.5×10^{-15}	1.2×10^{-15}	5.9×10^{-16}
$j_{\rm B}$ (cgs)	3.3×10^{-4}	2.6×10^{-4}	1.2×10^{-4}	1.1×10^{-4}
B (G)	210	150	52	44
E_0 (statV cm^{-1})	1.5×10^{-5}	1.3×10^{-5}	9.0×10^{-6}	8.7×10^{-6}
$\lambda_{\rm p}/{\rm r_g}$	1.3×10^{-7}	1.5×10^{-7}	2.2×10^{-7}	2.3×10^{-7}
$\gamma_{\rm p}$	1.5×10^{6}	1.5×10^{6}	2.9×10^{6}	6.4×10^{6}
$E_{\parallel}/E_0$	750	780	1300	2200
$E_{\parallel}$ (statV cm^{-1})	0.011	0.010	0.011	0.019
$L_{\rm gap}$ (erg s^{-1}) ($1r_{\rm g}$ gap size)	1.3×10^{41}	8.6×10^{40}	2.1×10^{40}	2.2×10^{40}

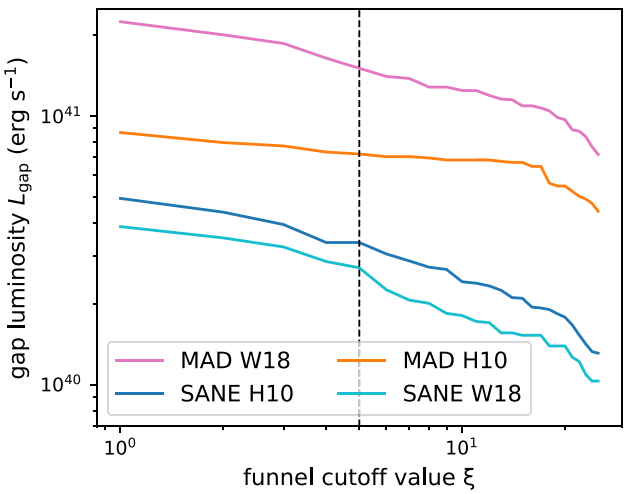

Figure 12. Time-averaged gap luminosity ($L_{\rm gap}$) near the null surface around $r \simeq 2r_{\rm g}$ as a function of ξ, where $\sigma \geq \xi$ defines the funnel region. The dashed line marks our choice of $\xi = 5$ for defining the funnel boundary.

dependent 1D PIC simulations to study particle acceleration due to gap formation in a black hole magnetosphere. They found that quasi-periodic operation of a gap in M87's near-horizon funnel region can produce TeV flares with intermittency similar to the observed variability time-scale. Drawing empirically from their simulation results, they developed an analytic model to estimate the parallel electric field strength and, in turn, the gap luminosity. Here, we will first recapitulate the simple analytic model, then use the physical quantities computed from our radiation GRMHD simulations as inputs to the model, considering the SANE and MAD accretion flows along with the H10 and W18 electron heating models.

Assuming charge carriers with number density n move at close to the speed of light, we can approximate the background current density $j_{\rm B} = enc$, which aids the estimation of the plasma frequency $\omega_{\rm p}$ and the plasma skin depth $\lambda_{\rm p}$ as follows:

$$\omega_{\rm p} = \sqrt{\frac{4\pi n e^2}{m_{\rm e}}} = \sqrt{\frac{4\pi e j_{\rm B}}{m_{\rm e} c}}, \quad \lambda_{\rm p} = \frac{c}{\omega_{\rm p}}. \tag{6}$$

Requiring each electron in E_0 to gain energy equal to $m_{\rm e}c^2$ after accelerating over a distance of $\lambda_{\rm p}$, this electric field unit is defined

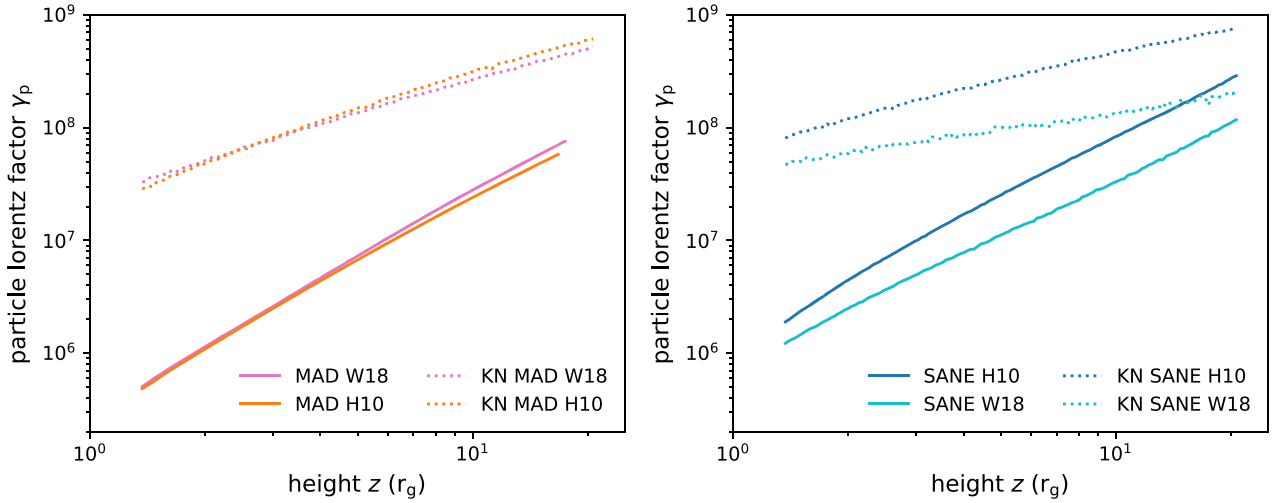

Figure 13. Time-averaged Lorentz factor (solid line) and associated Klein–Nishina limit $\gamma_p \sim 0.1/\epsilon_{min}$ (dotted line) are plotted against radius. MAD simulations with W18 (pink) and H10 (orange) schemes are on the left-hand panel; SANE simulations with W18 (cyan) and H10 (blue) schemes are on the right-hand panel.

as

$$E_0 = \frac{m_e c^2}{e\lambda_p} = \sqrt{\frac{4\pi j_B m_e c}{e}}. \quad (7)$$

Scattering with background soft photons generates γ-rays with κ of them converted into pairs within time t:

$$\kappa = \frac{c^2 t^2}{5\ell_{IC}^2}(\gamma_p^2 \epsilon_{min}^2)^\alpha \sim 10, \quad (8)$$

where $\alpha \sim 1.2$ is the spectral index, γ_p is the primary particle Lorentz factor, and ϵ_{min} is the minimum photon energy in units of $m_e c^2$. For the calculation of L_{gap}, we use an empirical power-law seed photon spectrum rather than the spectral shape found from our radiation GRMHD simulations. This choice is made both for consistency with the work of Chen et al. (2018), whose 1D GR PIC simulations assume a power-law distribution of seed photons, and because our current models do not accurately reproduce the infrared to X-ray SED shape observed from M87. New GR PIC calculations based on photon distributions from radiation GRMHD may find different pair cascade properties and gap luminosities.

For a gap height of $\sim 1\, r_g$,the gap electric field $E_{||}$ in units of E_0 can then be calculated as

$$\frac{E_{||}}{E_0} = \left(\frac{5\kappa \ell_{IC}^2}{8\pi\lambda_p r} \left(\frac{3(\alpha-1)}{4\alpha} \frac{\ell_{IC}\epsilon_{min}}{\lambda_p} \right)^{-\alpha} \right)^{1/(\alpha+1)}, \quad (9)$$

where $\ell_{IC} = 1/n_s\sigma_T$ is the mean-free path for an electron to undergo inverse-Compton scattering in the Thomson limit.

We assume a constant gap size h, and allow the gap to appear anywhere in the funnel between the horizon radius of 1.37 and $\sim 40 r_g$, where the photons are collected. We then calculate the gap luminosity as a function of its height above the black hole z as

$$L_{gap}(z) \simeq \pi \Delta x_2\, r_g^3 \frac{h}{r} \sum_k \sqrt{-g} E_{||,k}\, j_{B,k}. \quad (10)$$

Here, all variables are ϕ-averaged, and Δx_2 is related to the polar angle spacing in our simulation grid. In addition, the summation is done across the angular region at a given radius inside which $\sigma \geq 5$.

The Lorentz factors of accelerated particles are limited by inverse-Compton cooling, therefore they are determined by the acceleration $E_{||}$ and the scattering free path:

$$\gamma_p^2 = \frac{3eE_{||}(\alpha-1)\ell_{IC}}{4\alpha\epsilon_{min} m_e c^2}. \quad (11)$$

The model described above works well when inverse-Compton scattering occurs mostly in the Thomson regime, when $\gamma_p \lesssim 0.1/\epsilon_{min}$(Chen et al. 2018). In this regime, the scattered photon energy can be computed simply as

$$E_{ph} = 2\gamma_p^2 \epsilon. \quad (12)$$

We use the photon number density, radiation energy density, and current density from the simulation as inputs into the analytic model. All data are averaged over the final $\sim 2000\, r_g/c$ of each simulation. Fig. 11 shows the gap luminosity produced by the parallel electric field for a gap of size $h = 1 r_g$ as a function of the height z where it appears. MADs have a gap luminosity around 10^{41} erg s^{-1} in contrast to the value around 2×10^{40} erg s^{-1} for SANEs. The difference can be partially attributed to the higher product of $E_{||}$ and j_B and partially to the larger funnel size seen in MAD simulations. Varying the electron heating scheme results in much smaller differences. All four simulations show a decreasing trend of gap luminosity with distance from the horizon. Table 4 gives typical values of each simulation variable averaged over azimuthal and polar angle, between 2 and $3r_g$, and inside the defined funnel region. The choice of the critical value of σ to define the funnel boundary (ξ) leads to modest changes in the gap luminosity (Fig. 12).

All simulations are capable of producing TeV γ-ray photons depending on the radius at which the gap electric field emerges. As presented in Fig. 11, all trends suggest that for a gap appearing further away from the horizon, the produced gap luminosity decays while γ-ray photon energy increases, reaching TeV range (> 0.3 TeV) at approximately $3r_g$ for SANE simulations and $6r_g$ for MAD simulations. The Lorentz factors to boost to high energy shown in Fig. 13 are all below the corresponding Klein–Nishina limit where Chen et al. (2018)'s analytic model applies. However, we do not see significant flares in the time variability with only a dozen samplings. The simulation duration is limited by the computational expense of 3D radiation GRMHD.

5 DISCUSSION

We have presented 3D radiation GRMHD simulations of accretion on to the supermassive black hole in M87. The simulations were performed with the public code EBHLIGHT, which evolves the frequency-dependent radiation field using a Monte Carlo method. We have explored regimes of weak and dynamically important accumulated magnetic flux (SANE and MAD), as well as different subgrid prescriptions for electron heating from either turbulence (as realized in gyrokinetics calculations) or reconnection (as realized in PIC calculations). Radiative cooling lowers the average electron temperature by factors of $\simeq$ 2–5. For SANE models, our T_e maps are consistent with those from the axisymmetric `ebhlight` calculations of Ryan et al. (2018). MAD models using the H10 prescription show higher T_e and much stronger radiation pressure in the funnel than when using the W18 or R17 prescriptions. This finding agrees with that of Chael et al. (2019), and is even more pronounced in a short MAD H10 run where we included radiation for $\sigma < 25$. However, those changes do not seem to play a major role in influencing the accretion flow dynamics (but see Chael et al. 2019). Spectra from synchrotron radiation and inverse-Compton scattering from a purely thermal electron distribution can reproduce the radio/submillimeter and in some cases X-ray luminosity of M87.

The choice of electron heating prescription in combination with the SANE or MAD state leads to different electron temperature distributions, and in turn the relative importance of inverse-Compton scattering (e.g. the y-parameter). The gyrokinetic turbulence prescriptions (H10 and K19) produce colder electrons in the accretion flow body, resulting in lower scattered luminosities especially in the SANE case. The high density and disc electron temperature in the parameter combinations of SANE with reconnection heating (W18 and R17) result in the models systematically overproducing the observed X-ray luminosity. The MAD models are already radiatively efficient at low luminosity ($L_{\rm bol}/\dot{M}c^2 \approx 10$ per cent), while the efficiencies of the SANE models are roughly an order of magnitude smaller. All radiative efficiencies are about an order of magnitude larger than in similar, non-radiative simulations of Sgr A$*$ (Dexter et al. 2020).

We use the simulations to study the radiation and magnetic field properties in the evacuated, jet funnel region. The funnel is systematically wider in the MAD case, consistent with past results. The radiation field is generally anisotropic, and the relative preferred photon direction varies systematically with height above the black hole from ingoing near the horizon to outgoing for $r \gtrsim 6\,r_g$. This result can be explained in terms of the compact, near equatorial emission regions in our simulations.

By comparing a rough estimate of the funnel pair-production rate with the Goldreich–Julian density, it appears that the charge density in the funnel may be high enough to screen the electric fields. However, the strong dependence of the pair-production rate with mass accretion rate suggests that a moderate change in accretion flow properties could, in principle. trigger gap formation and particle acceleration in the funnel. We use radiation and magnetic field quantities from our simulations (Table 4) to estimate $L_{\rm gap}$ using Chen et al. (2018)'s models, assuming a gap is able to form

$$L_{\rm gap} \sim E_{||}\, j_{\rm B} r_{\rm g}^3 \sim \frac{E_{||}}{B} L_{\rm jet}, \tag{13}$$

which provides a consistent estimate of $L_{\rm gap}$ for a jet power of $\sim 10^{43}\,{\rm erg\,s^{-1}}$. The resulting gap luminosity varies between $10^{40}\,{\rm erg\,s^{-1}}$ to a few times $10^{41}\,{\rm erg\,s^{-1}}$, depending on the electron heating scheme, with SANE simulations providing much closer values to Chen et al. (2018)'s estimates of $\sim 2 \times 10^{40}\,{\rm erg\,s^{-1}}$. This fits most of the predictions from various simulation processes and assumptions (Chen & Yuan 2020; Katsoulakos & Rieger 2020), as well as reported observational evidence of M87's VHE flares with $L_{\rm VHE} \simeq (0.8\text{–}2.4) \times 10^{42}\,{\rm erg\,s^{-1}}$ (Abramowski et al. 2012). Compared with the earlier work by Broderick & Tchekhovskoy (2015), the PIC models that we use generally predict lower total gap luminosity, especially at high optical depth τ_0. This is because pair production through photon collision becomes very efficient and the gap is quickly screened. Broderick & Tchekhovskoy (2015) found that the γ-ray luminosity from the gap can be very high ($\sim 10^{43}\,{\rm erg\,s^{-1}}$), but most of it is beamed away from us. Our model does not require this assumption, but a future more careful examination of radiation beaming in the presence of the magnetic field structure from GRMHD simulations may be useful to further constrain the observed γ-ray luminosity.

Recently Kisaka et al. (2020a) also performed 1D GR PIC simulations of gaps. They focused on the regime where the fiducial optical depth τ_0 is between 10 and 300 and concluded that the luminosity of curvature radiation from the accelerated particles can dominate the high-energy emission in some models. In this work, we have found that the optical depth in the vicinity of M87 can be much higher, $\tau_0 \sim 10^5$. In this regime, inverse-Compton cooling is much more efficient, limiting the particles to lower Lorentz factors. Since the luminosity of curvature radiation scales as γ^4, it becomes subdominant in producing high-energy γ-rays.

We have assumed a uniform gap size of $h = 1r_g$ in our estimates. The gap size likely has a weak dependency on the optical depth τ_0 and the spectrum of the soft photons. A recent work by Crinquand et al. (2020) showed that in an axisymmetric configuration, under a mono-energetic soft photon background, the gap can be very narrow, $h \sim 0.05 r_g$. A more systematic study to understand the scaling of the gap size with geometry, optical depth, and the background photon distribution will help to improve upon our estimates for the gap luminosity.

We only see a small variability of the gap luminosity from our simulations by factors of $\lesssim 2$, which is insufficient to explain the large amplitude of VHE flaring observed from M87. Variability properties would be interesting to study in longer duration radiation GRMHD simulations with a higher dump cadence. Our preliminary results suggest that flares might instead require a large-scale change to the funnel structure or jet power, or alternatively could be triggered by small-scale kinetic processes within the funnel region itself.

ACKNOWLEDGEMENTS

We thank M. C. Begelman, C. F. Gammie, A. Philippov, A. Tchekhovskoy, and D. Uzdensky for helpful discussions, and the referee, A. Chael, for constructive comments that improved this paper. This work was supported in part by NASA Astrophysics Theory Program grant 80NSSC20K0527, an Alfred P. Sloan Research Fellowship, a Sofja Kovalevskaja award from the Alexander von Humboldt foundation, a Donald C. and F. Shirley Jones Fellowship, and the Undergraduate Research Opportunities Program (UROP) at the University of Colorado Boulder. The calculations presented here were carried out on the MPG supercomputer Cobra hosted at MPCDF and used resources supported by the NASA High-End Computing (HEC) Program through the NASA Advanced Supercomputing (NAS) Division at Ames Research Center. This work has been assigned a document release number LA-UR-21-21285.

DATA AVAILABILITY

The simulation data analysed in this paper will be shared on reasonable request to the corresponding author.

REFERENCES

Abramowski A. et al., 2012, ApJ, 746, 151
Acciari V. A. et al., 2009, Science, 325, 444
Aharonian F. et al., 2006, Science, 314, 1424
Akiyama K. et al., 2015, ApJ, 807, 150
Balbus S. A., Hawley J. F., 1991, ApJ, 376, 214
Bardeen J. M., Press W. H., Teukolsky S. A., 1972, ApJ, 178, 347
Biretta J. A., Sparks W. B., Macchetto F., 1999, ApJ, 520, 621
Blandford R. D., Znajek R. L., 1977, MNRAS, 179, 433
Breit G., Wheeler J. A., 1934, Phys. Rev., 46, 1087
Broderick A. E., Tchekhovskoy A., 2015, ApJ, 809, 97
Chael A., Narayan R., Johnson M. D., 2019, MNRAS, 486, 2873
Chen A. Y., Yuan Y., 2020, ApJ, 895, 121
Chen A. Y., Yuan Y., Yang H., 2018, ApJ, 863, L31
Crinquand B., Cerutti B., Philippov A. e., Parfrey K., Dubus G., 2020, Phys. Rev. Lett., 124, 145101
Davelaar J. et al., 2019, A&A, 632, A2
De Villiers J.-P., Hawley J. F., Krolik J. H., 2003, ApJ, 599, 1238
Dexter J., McKinney J. C., Agol E., 2012, MNRAS, 421, 1517
Dexter J. et al., 2020, MNRAS, 494, 4168
Di Matteo T., Allen S. W., Fabian A. C., Wilson A. S., Young A. J., 2003, ApJ, 582, 133
Dibi S., Drappeau S., Fragile P. C., Markoff S., Dexter J., 2012, MNRAS, 426, 1928
Doeleman S. S. et al., 2012, Science, 338, 355
Drappeau S., Dibi S., Dexter J., Markoff S., Fragile P. C., 2013, MNRAS, 431, 2872
Event Horizon Telescope Collaboration et al., 2019a, ApJ, 875, L4
Event Horizon Telescope Collaboration et al., 2019b, ApJ, 875, L5
Event Horizon Telescope Collaboration et al., 2019c, ApJ, 875, L6
Gammie C. F., McKinney J. C., Tóth G., 2003, ApJ, 589, 444
Gebhardt K., Adams J., Richstone D., Lauer T. R., Faber S. M., Gültekin K., Murphy J., Tremaine S., 2011, ApJ, 729, 119
Hada K., Doi A., Kino M., Nagai H., Hagiwara Y., Kawaguchi N., 2011, Nature, 477, 185
Howes G. G., 2010, MNRAS, 409, L104 (H10)
Junor W., Biretta J. A., Livio M., 1999, Nature, 401, 891
Katsoulakos G., Rieger F. M., 2020, ApJ, 895, 99
Kawazura Y., Barnes M., Schekochihin A. A., 2019, Proc. Natl. Acad. Sci., 116, 771 (K19)
Kisaka S., Levinson A., Toma K., 2020a, ApJ, 902, 80
Kisaka S., Levinson A., Toma K., 2020b, ApJ, 902, 80
Kuo C. Y. et al., 2014, ApJ, 783, L33
Levinson A., Cerutti B., 2018, A&A, 616, A184
Levinson A., Rieger F., 2011, ApJ, 730, 123
Liska M., Hesp C., Tchekhovskoy A., Ingram A., van der Klis M., Markoff S., 2018, MNRAS, 474, L81
McKinney J. C., Tchekhovskoy A., Blandford R. D., 2012, MNRAS, 423, 3083
Mignone A., McKinney J. C., 2007, MNRAS, 378, 1118
Miller J. M. et al., 2019, Phys. Rev. D, 100, 023008
Mościbrodzka M., Gammie C. F., Dolence J. C., Shiokawa H., 2011, ApJ, 735, 9
Mościbrodzka M., Falcke H., Shiokawa H., 2016, A&A, 586, A38
Narayan R., Sadowski A., Penna R. F., Kulkarni A. K., 2012, MNRAS, 426, 3241
Noble S. C., Gammie C. F., McKinney J. C., Del Zanna L., 2006, ApJ, 641, 626
Perlman E. S., Sparks W. B., Radomski J., Packham C., Fisher R. S., Piña R., Biretta J. A., 2001, ApJ, 561, L51
Porth O. et al., 2019, ApJS, 243, 26
Prieto M. A., Fernández-Ontiveros J. A., Markoff S., Espada D., González-Martín O., 2016, MNRAS, 457, 3801
Ressler S. M., Tchekhovskoy A., Quataert E., Chand ra M., Gammie C. F., 2015, MNRAS, 454, 1848
Ressler S. M., Tchekhovskoy A., Quataert E., Gammie C. F., 2017, MNRAS, 467, 3604
Reynolds C. S., Di Matteo T., Fabian A. C., Hwang U., Canizares C. R., 1996, MNRAS, 283, L111
Rowan M. E., Sironi L., Narayan R., 2017, ApJ, 850, 29 (R17)
Ryan B. R., Dolence J. C., Gammie C. F., 2015, ApJ, 807, 31
Ryan B. R., Ressler S. M., Dolence J. C., Tchekhovskoy A., Gammie C., Quataert E., 2017, ApJ, 844, L24
Ryan B. R., Ressler S. M., Dolence J. C., Gammie C., Quataert E., 2018, ApJ, 864, 126
Ryan B. R., Dolence J. C., Gammie C. F., Ressler S. M., Miller J., 2019, Astrophysics Source Code Library, record ascl:1909.007
Tchekhovskoy A., 2019, Astrophysics Source Code Library, record ascl:1912.014
Tchekhovskoy A., Narayan R., McKinney J. C., 2011, MNRAS, 418, L79
Tully R. B., 1988, Nearby Galaxies Catalogue, Cambridge Univ. Press, Cambridge
Walker R. C., Hardee P. E., Davies F. B., Ly C., Junor W., 2018, ApJ, 855, 128
Werner G. R., Uzdensky D. A., Begelman M. C., Cerutti B., Nalewajko K., 2018, MNRAS, 473, 4840 (W18)
White C. J., Dexter J., Blaes O., Quataert E., 2020, ApJ, 894, 12
Wielgus M. et al., 2020, ApJ, 901, 67
Wong G. N., Ryan B. R., Gammie C. F., 2021, ApJ, 907, 73
Yarza R., Wong G. N., Ryan B. R., Gammie C. F., 2020, ApJ, 898, 50

APPENDIX A: CONVERGENCE TESTS

To test for convergence of the radiation field, we compare shell-averaged radial profiles of various radiation quantities using different average numbers of superphotons in our MAD H10 simulation (Fig. A1). We expect a converged solution when a sufficient number of superphotons are used in the calculation. The solutions are nearly identical between our fiducial resolution and twice the number of superphotons. Using half the number results in larger radiation pressures and integrated cooling rates. The EBHLIGHT radiation quality factor $\langle Q_{\rm emit}\rangle$ is $\gtrsim 10$ for the fiducial case and $\gtrsim 30$ when using twice the number of superphotons. It falls below 1 in the lower resolution case. Based on our results, it seems that values $\langle Q_{\rm emit}\rangle \lesssim 10$ may indicate insufficient superphoton resolution.

For all simulations presented here, the *scattering* quality factor $\langle Q_{\rm scat}\rangle$ is $\ll$10 for small radii $r \lesssim 3\,r_{\rm g}$. This indicates that the inverse-Compton cooling may be inaccurate near the event horizon. Since $L_{\rm scat} \simeq L_{\rm emit}$ in many of our simulations (Table 2), a large value of $\langle Q_{\rm emit}\rangle$ may be insufficient to assess convergence. Fig. A2 shows the results of running the MAD W18 simulation (where $L_{\rm scat}/L_{\rm emit} \simeq 1$) with much higher superphoton resolution than in our fiducial simulations. The scattering quality factor increases with increasing number of superphotons as expected. The electron temperature varies slightly at small radius. The small magnitude of the variations, seen in all radiation variables as well as the observed spectra, suggests that underresolving scattering interactions may not compromise our radiation field solutions.

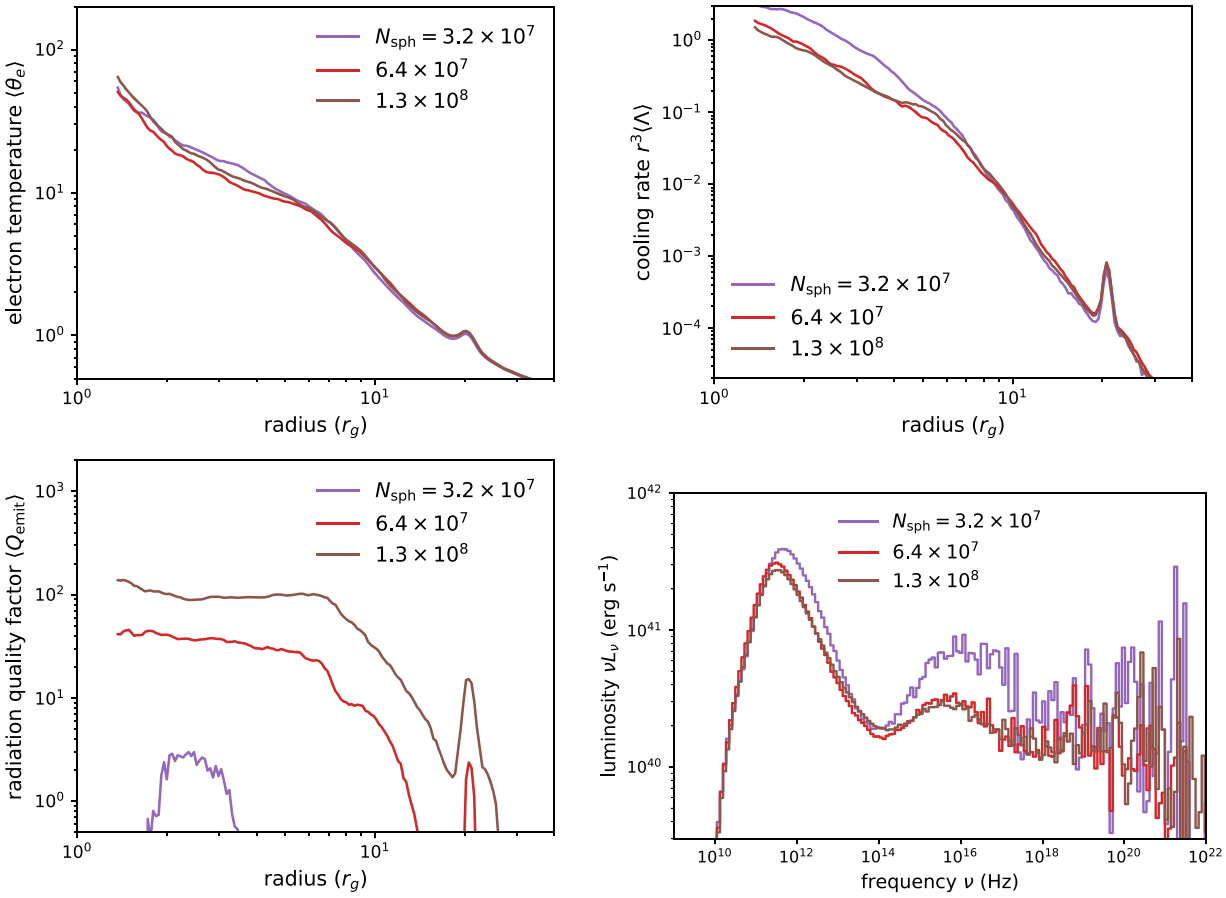

Figure A1. Electron temperature (top left-hand panel), integrated cooling rate (top right-hand panel), emission quality factor (bottom left-hand panel), and time-averaged SEDs (right-hand panel) as a function of the number of superphotons used for the MAD H10 model. Our fiducial resolution of 6.4×10^7 superphotons (approximately five to ten times the number of fluid grid zones) gives similar time-averaged results as using twice that number. The radiation quantities begin to diverge at half the fiducial number. The quality of the radiation solution seems well captured in this case by the quality factor $\langle Q_{\rm emit}\rangle$.

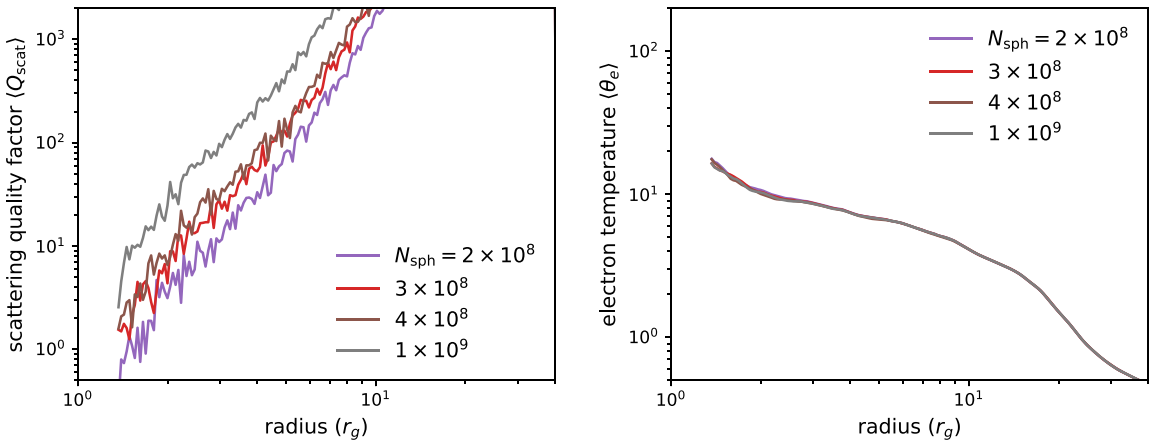

Figure A2. Scattering quality factor (left-hand panel) and electron temperature (right-hand panel) as a function of the number of superphotons used for the MAD W18 simulation. The numbers of superphotons used for this test are $\simeq$ 3–15 times larger than in our fiducial simulations. The scattering quality factor increases with superphoton resolution, and the electron temperature (and other radiation field dependent variables), appear well converged. This suggests that our low values of $\langle Q_{\rm scat}\rangle$ may not severely compromise the accuracy of the radiation field solution very close to the horizon ($r \lesssim 3\,r_{\rm g.}$).

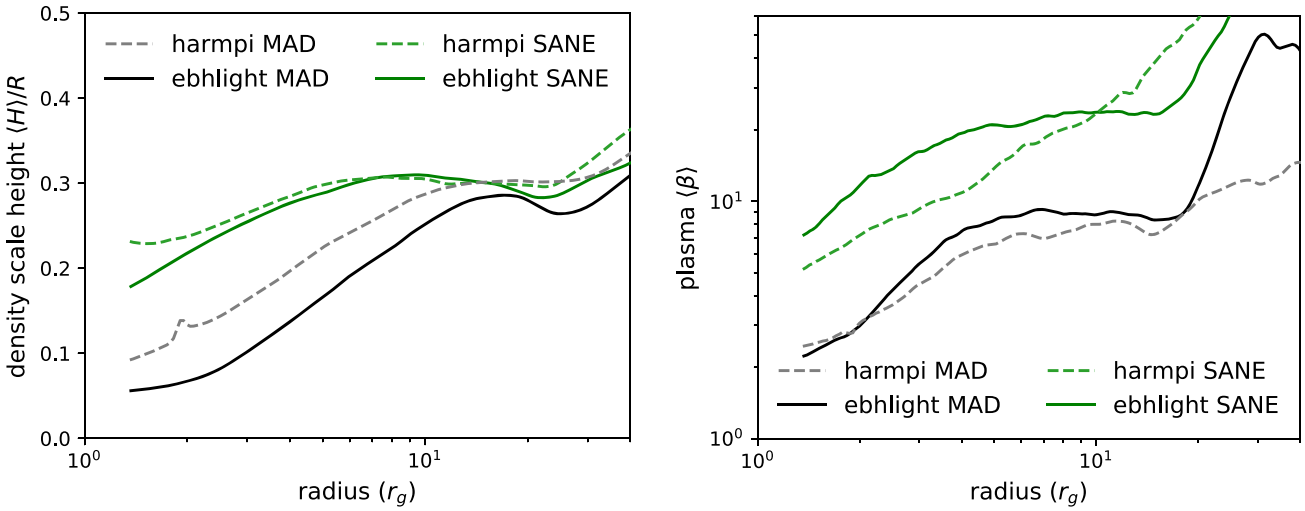

Figure B1. Comparison of radial profiles of $\langle H \rangle / R$ and plasma β for MAD and SANE flow solutions obtained using the EBHLIGHT and HARMPI codes averaged from 5500 to $-6500\, r_g/c$.

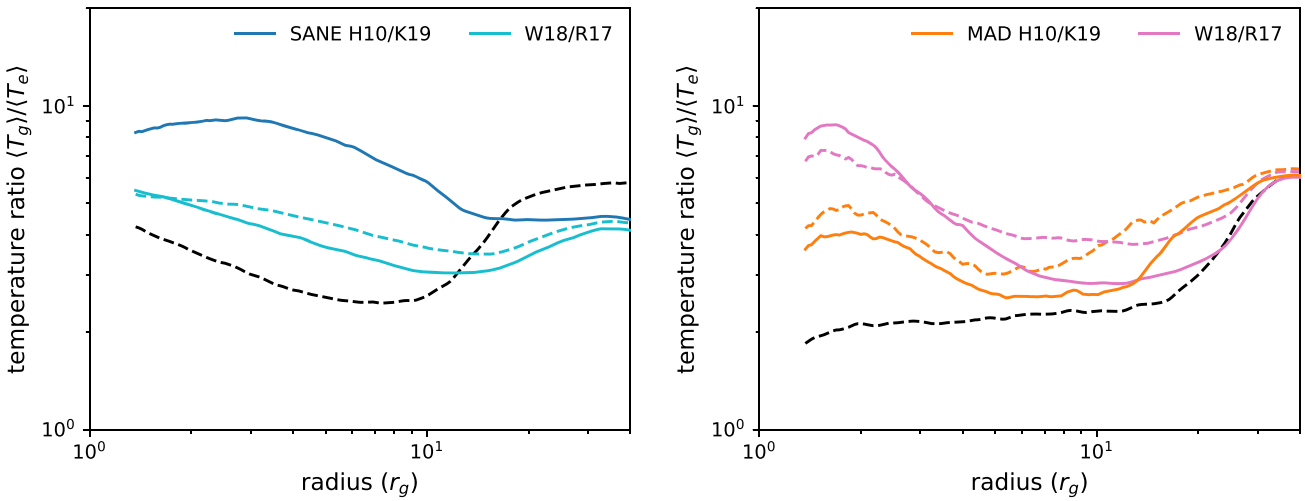

Figure B2. Total fluid to electron temperature ratio for our SANE (left) and MAD (right) simulations. The dashed black lines show the initial state before the radiation field is turned on. Electron cooling is important in all models studied—the temperature ratio increases for $r \lesssim 10\, r_g$ in all cases.

APPENDIX B: COMPARISON WITH GRMHD AND IMPORTANCE OF COOLING

Fig. B1 compares time-averaged radial profiles of density scaleheight and plasma β of SANE and MAD simulations obtained here with the W18 electron heating model and those from non-radiative simulations using the HARMPI code[3] (Tchekhovskoy 2019; Dexter et al. 2020). In both cases, the pairs of MAD and SANE simulations look similar. The density scaleheight from the HARMPI calculation is somewhat higher than with EBHLIGHT, while plasma β is somewhat larger in the EBHLIGHT SANE model than found with HARMPI. Note that the initial conditions are not identical between these cases, and additionally the EBHLIGHT simulations used an adiabatic index of 13/9, while the HARMPI simulations used 5/3. The choice of adiabatic index is known to cause differences in GRMHD calculations (e.g. Mignone & McKinney 2007; White et al. 2020).

Fig. B2 compares the shell-averaged total fluid to electron temperature ratios for pure GRMHD (dashed black lines) to data from after the radiation is turned on (solid lines). The temperature ratio increases once radiative cooling is turned on, particularly at very small radii where most of the luminosity is emitted. The density-weighted temperature ratios are highest for the SANE H10/K19 and MAD W18/R17 models. Radiative cooling changes the electron temperatures near the horizon by factors of $\simeq$ 2–5 on average.

[3] https://github.com/atchekho/harmpi.

This paper has been typeset from a TEX/LATEX file prepared by the author.